RSC Advances

PAPER

View Article Online
View Journal | View Issue

Cite this: *RSC Adv.*, 2025, **15**, 30312

Mechanistic insights into coke suppression in the methanol-to-olefins process *via* CeO_2 doping to SAPO-34

Armin Abbasi, Jafar Towfighi Darian, * Mohammad Javad Emami and Masoud Safari Yazd *

This study provides novel mechanistic insights into the transformative role of cerium oxide (CeO_2) incorporation into SAPO-34 for the methanol-to-olefins (MTO) process. By integrating experimental findings with molecular dynamics (MD) simulations, the work elucidates specific pathways through which CeO_2 mitigates coke formation. MD simulations reveal that CeO_2 suppresses the formation of CHO-θ intermediates, key precursors to coke, while enhancing coke removal through improved CO_2 activation and the Boudouard reaction. Catalytic testing corroborates these findings, demonstrating enhanced durability for up to 600 min and a total olefin selectivity of up to 83.9%. Structural and chemical modifications, such as reduced crystallite size, increased mesoporosity, and redistributed acid sites, were characterized using advanced techniques (XRD, FT-IR, FESEM, and NH_3-TPD). These modifications optimize the balance between weak and strong acid sites, facilitating efficient methanol conversion and olefin production. The integration of mechanistic insights with experimental results underscores the innovative role of CeO_2 in improving SAPO-34's catalytic efficiency, selectivity, and operational stability, establishing SP-Ce as a cutting-edge catalyst for industrial MTO applications.

Received 29th June 2025
Accepted 18th August 2025

DOI: 10.1039/d5ra04614a

rsc.li/rsc-advances

1. Introduction

As global demand for essential petrochemicals like ethylene and propylene grows, the Methanol-to-Olefins (MTO) process has emerged as a sustainable alternative to petroleum-based production. This process uses methanol-a versatile feedstock that can be sourced from renewable resources, such as biomass-to promote energy diversification and reduce dependence on crude oil. A critical component of the MTO process is the SAPO-34 catalyst, a chabazite-type material known for its high selectivity in converting methanol to light olefins. Its unique microporous structure, featuring 8-membered ring (8-MR) channels, is optimized for light olefin production, making SAPO-34 valuable for sustainable petrochemical manufacturing. To meet the rising demand for olefinic feedstocks like ethene, enhancing MTO catalysts is essential.[1–4]

However, SAPO-34 faces deactivation due to coke formation, as carbon-rich deposits block active sites and reduce catalytic efficiency. To mitigate this, researchers are reducing SAPO-34 crystal size and designing hierarchical pore structures to improve mass transport and diffusion. These advancements extend SAPO-34's catalytic lifespan, reinforcing its efficiency in olefin production. Recent studies highlight formaldehyde (HCHO) as a key coke precursor in the MTO reaction. Formed early in the process, formaldehyde condenses on SAPO-34 and interacts with other intermediates, producing aromatics through mechanisms like the Prins reaction, which accelerates deactivation.[3,5–10]

Formaldehyde is generated through pathways such as methanol disproportionation, thermal decomposition, and hydride transfer at Lewis acid sites. It reacts with olefins to produce dienes and aromatics, both of which promote coke buildup. Even trace amounts of formaldehyde can accelerate coke formation and catalyst deactivation, shifting selectivity toward aromatics and leading to increased coke deposition.[5,11] Controlling formaldehyde concentration is essential to minimize coke formation and prolong catalyst life. Strategies include diluting methanol, co-feeding alkenes, and back-mixing to recycle products, which reduces methanol's chemical potential and lowers formaldehyde levels. Additionally, using dimethyl ether (DME) as feedstock has shown potential, as it bypasses certain pathways that lead to formaldehyde formation.[5–7,11,12] In contrast, adding metal oxides to SAPO-34 has proven effective in mitigating formaldehyde-driven coking, enhancing catalyst stability and MTO efficiency.[5,13]

The incorporation of metal oxides in SAPO frameworks is crucial for improving catalysis in hydrocarbon conversion.[13] Transition metal ions, introduced *via* isomorphous substitution, create active sites that enhance catalytic performance. Their behavior is influenced by their location in the porous

Faculty of Chemical Engineering, Department of Process, Tarbiat Modares University, P. O. Box: 14115-143, Tehran, Iran. E-mail: towfighi@modares.ac.ir; masoud.safari@modares.ac.ir

structure, such as near 6- and 10-ring windows. Characterization methods reveal interactions between metal ions and reactants, deepening our understanding of catalytic mechanisms. Research on transition metals shows promise for optimizing SAPO materials to reduce deactivation and improve efficiency in specific applications.[13–15]

In addition, metal oxides in SAPO materials, such as H-SAPO-34 and SAPO-18, significantly affect catalytic behavior.[16] For example, adding nickel enhances selectivity for ethene, with nickel-containing SAPO-34 achieving nearly 90% ethene yield with stable, long-term performance. This selectivity results from interactions between metal ions and reaction intermediates, which modify acidity and product distribution. Therefore, refining metal oxide types and concentrations in SAPO frameworks is critical for increasing olefin production efficiency.[14] Metal oxides stabilize intermediates, influencing reaction pathways and boosting yields, making a thorough understanding of these roles essential for optimizing MTO catalysts and enhancing olefin production efficiency.[17,18]

Some contradictory reports exist. For instance, ZnO has been reported in some studies as an important component in reducing coke formation in MTO reactions by enhancing selectivity and stabilizing catalysts.[19] ZnO suppresses paraffin formation, favoring propylene and lighter hydrocarbons over coke-promoting paraffins.[15] Although ZnO improves the ethene-to-propene ratio, highlighting the complex role of metal oxides in MTO reactions, other studies have reported that it promotes coke deposition.[20,21] Studies, such as those by Cordero-Lanzac *et al.*,[22] demonstrate that ZnO paired with MgO/SAPO-18 (MgAPO-18) reduces heavy hydrocarbon intermediates that might otherwise polymerize into coke on acid sites. The structural and electronic characteristics of metal oxides enable selective interactions with SAPO active sites, promoting reactions that avoid polyaromatic formation and prevent catalyst deactivation. Additionally, bifunctional catalysts have advanced syngas-to-olefin conversion by transforming intermediates on metal oxide surfaces. For instance, Y_2O_3 decomposes formaldehyde, which initiates and terminates chain growth in the MTO process, thereby limiting coke accumulation.[23] On the other hand, other studies have emphasized[24–26] that metal oxides play a vital role in reducing coke formation in MTO reactions through other strategies, including reducing crystal size and introducing meso- or macropores to prevent catalyst deactivation.

While pairing metal oxides with SAPO zeolites of strong acidity and selectivity has been widely acknowledged to diminish coke precursors and extend catalyst longevity,[22] understanding the mechanistic role of these oxides in reducing coke formation remains crucial, particularly in prominent cases. Among these, incorporating rare-earth elements like cerium (Ce) into SAPO-34 has shown significant promise, though it has received relatively little attention. Cerium modifies the porosity and acidity of the catalyst, thereby enhancing its performance and lifetime. Recent findings demonstrate that a physical mixture of SSZ-13 and ceria (CeO_2) extends catalyst lifetimes in MTO reactions compared to pure SSZ-13. This improvement is attributed to formaldehyde decomposition on CeO_2 surfaces, likely proceeding through formate intermediates, which mitigates coke formation. Moreover, the morphology of CeO_2 significantly influences catalyst stability, underscoring the importance of optimizing metal oxide structures to achieve superior catalytic performance.[23,27,28]

Ceria's exceptional redox properties, including its ability to alternate between Ce^{3+} and Ce^{4+} oxidation states and its high oxygen storage capacity (OSC), make it a valuable addition to SAPO-34 catalysts for the MTO process. By regulating oxygen concentration through oxygen vacancy defects, ceria can stabilize critical intermediates like methoxy under reaction conditions, directing them toward favorable olefin products while suppressing the formation of undesirable species such as formaldehyde. These reactive sites enhance methanol conversion to olefins, minimizing the accumulation of coke precursors and by-products.[27] Additionally, ceria's redox flexibility facilitates oxidation cycles within the catalyst, promoting resistance to deactivation. Its oxygen mobility enables the oxidation of coke precursors, either through direct redox reactions or by facilitating the reverse Boudouard reaction, thereby preserving active sites and extending the catalyst's operational lifespan. Furthermore, ceria aids in the spillover of reactants like H_2 and CO, supporting secondary reactions that improve olefin yield and overall MTO efficiency.[27,29]

In this regard, this study provides a comprehensive evaluation of the effects of ceria incorporation into SAPO-34 in the MTO process, combining experimental and theoretical approaches. Molecular dynamic (MD) simulations are employed to elucidate the mechanistic pathways by which cerium oxide reduces coke precursors or mitigates their formation. In parallel, catalytic testing is conducted to validate the performance improvements. Additionally, advanced characterization techniques are applied to investigate the structural and chemical modifications in SAPO-34 resulting from ceria integration, offering deeper insights into its catalytic behavior and performance enhancement mechanisms.

2. Experimental and theoretical approach

2.1. Catalyst preparation

The synthesis of SAPO-34 catalysts involves using tetraethylammonium hydroxide (TEAOH, 20 wt%) and morpholine (Mor, 99%) as organic template agents, with aluminum isopropoxide (AIP, 99 wt%), phosphoric acid (H_3PO_4, 85 wt%), and tetraethyl orthosilicate (TEOS, $C_8H_{20}O_4Si$) serving as the sources of aluminum, phosphorus, and silicon, respectively. The molar composition used for synthesis is $1Al_2O_3 : 1P_2O_5 : 0.6SiO_2 : 1.25TEAOH : 1.25Mor : 70H_2O$.[4,30]

To begin, aluminum iso-propoxide is dissolved in deionized water. Tetraethylammonium hydroxide and morpholine are then added dropwise to this solution, forming a white gel, which is stirred for 1 hour at room temperature. Following this, tetraethyl orthosilicate is introduced dropwise into the mixture, with stirring continued for 3 hours at 60 °C. Afterward, phosphoric acid is carefully added dropwise, and the solution is

stirred for an additional 2 hours at the same temperature. The resulting mixture is aged at room temperature for 24 hours to allow the components to interact fully.

For Ce-doped SAPO-34 synthesis, cerium nitrate hexahydrate, in a ratio of 0.05 relative to Al_2O_3,[13] is dissolved in water and added to the gel mixture along with aqueous ammonium carbonate. Both solutions are introduced dropwise simultaneously. This modified gel mixture, along with the non-doped version, undergoes hydrothermal treatment at 180 °C for 24 hours in a stainless-steel autoclave.

After hydrothermal treatment, the solid products are separated by centrifugation, thoroughly washed with deionized water, and dried at 100 °C for 12 hours. The dried samples are then calcined at 550 °C for 5 hours to remove any residual organic templates. The final Ce-doped catalyst is designated as SP-Ce, whereas the undoped SAPO-34, synthesized by the same procedure but without adding cerium nitrate, is labeled as SP.

2.2. Characterization methods

A range of advanced characterization techniques is employed to investigate the impact of chemical modifications on the performance of SAPO-34 in the MTO process. Crystallinity and phase purity are analyzed through X-ray powder diffraction (XRD) using a Philips X'Pert MPD instrument. The measurements are taken within a 2θ range of 5–50, utilizing a Cu K_α radiation source ($\lambda = 1.54056$ Å). Fourier Transform Infrared Spectroscopy (FT-IR) is used to identify functional groups within the samples, performed on a PerkinElmer Spectrum Two spectrometer over the wavelength range of 400–4000 cm^{-1}.

The morphological characteristics of the samples are examined using a TESCAN MIRA3 field emission scanning electron microscope (FESEM). This instrument is also equipped with an energy-dispersive X-ray spectrometer (EDS) to determine the surface elemental composition. Textural properties, such as surface area and pore volume, are evaluated through nitrogen adsorption/desorption isotherms at 77 K, using a Micromeritics Tristar 3020 automated analyzer. To assess the acidic properties, NH_3-TPD analysis is performed with a BELCAT-B catalyst analyzer fitted with a thermal conductivity detector (TCD). Fresh samples (50 mg each) are pretreated at 500 °C for 1 hour under helium flow, then cooled and exposed to ammonia at 100 °C. Afterward, temperature-programmed desorption profiles are recorded as the temperature is increased from 100 to 700 °C at a rate of 10 °C min^{-1} under helium flow.

These comprehensive analyses provide insights into the structural, functional, morphological, and chemical properties of SAPO-34 and their implications for catalytic performance.

2.3. MD simulation overview

MD simulation is a computational technique used to analyze the time-dependent behavior of atoms and molecules at the nanoscale. By solving equations of motion, it predicts atomic evolution over time, employing the velocity Verlet algorithm to accurately calculate atomic positions and velocities within the simulation framework. This method enables the determination of critical properties, such as activation energy barriers, providing detailed atomistic insights into interatomic and intermolecular interactions. These insights are particularly valuable for understanding and predicting the behavior of cerium oxide supported on SAPO-34 in the MTO process. The reliability of MD simulations hinges on the accuracy of the interatomic potentials or force fields employed, as well as the accurate representation of the system and simulation conditions. In this study, the Universal Force Field (UFF) is utilized, incorporating the Lennard-Jones (LJ) potential to model nonbonded interactions:[31]

$$\phi(r_{ij}) = 4\varepsilon\left[\left(\frac{\sigma}{r_{ij}}\right)^{12} + \left(\frac{\sigma}{r_{ij}}\right)^{6}\right];\ r_{ij} \ll r_c \quad (1)$$

Key parameters include ε (the depth of the interaction energy well), σ (the distance at which the interaction potential becomes zero), and r_{ij} (the distance between atoms i and j), with a cutoff distance (r_c) of 12 Å applied for all atom types.

Bonded interactions, such as bond stretching and angle bending, are described using harmonic potential formalisms characterized by oscillator constants (k_r and k_θ) and equilibrium parameters (r_0 and θ_0), as expressed in the relevant equations. Dihedral interactions are also represented through harmonic potentials, ensuring a comprehensive modeling of the atomic and molecular behavior.

$$E = \tfrac{1}{2}k_r(r - r_0)^2 \quad (2)$$

$$E = \tfrac{1}{2}k_\theta(\theta - \theta_0)^2 \quad (3)$$

Two distinct ensembles are utilized to define the initial conditions for the simulations. The NVT ensemble maintains a constant temperature, volume, and particle number, while the NPT ensemble regulates both pressure and temperature during the atomic arrangement phase. Thermal equilibrium is achieved using the Nose–Hoover thermostat within 10 ns, followed by an additional 10 ns of simulation to ensure system convergence. The simulations are conducted using the LAMMPS computational package. The computational box is defined with dimensions of 350 × 350 × 350 $Å^3$, and periodic boundary conditions are applied. The Nose–Hoover thermostat and barostat are employed to maintain stability, with a damping ratio of 1 for temperature and 10 for pressure. Simulations are performed under an initial temperature of 300 K and an initial pressure of 1 atm. A time step of 0.01 femtoseconds is used to ensure precise calculations. The MD algorithms follow the NPT–NVT sequence to systematically adjust system parameters.[32,33] A visualization of the atomic arrangement at the initial stage of the simulations is provided in Fig. 1, offering insight into the starting configuration of the modeled structure.

In our computational workflow, the initial and final states of each target reaction ((R1)–(R6) as described in Section 3.1.5) are modeled as separate configurations. Classical MD simulations, performed in the NPT ensemble at 298 K using Newton's equations of motion with the velocity Verlet algorithm, are employed solely to thermally equilibrate these systems under realistic conditions. This low-temperature equilibration ensures structural stability and minimizes thermal noise prior to further

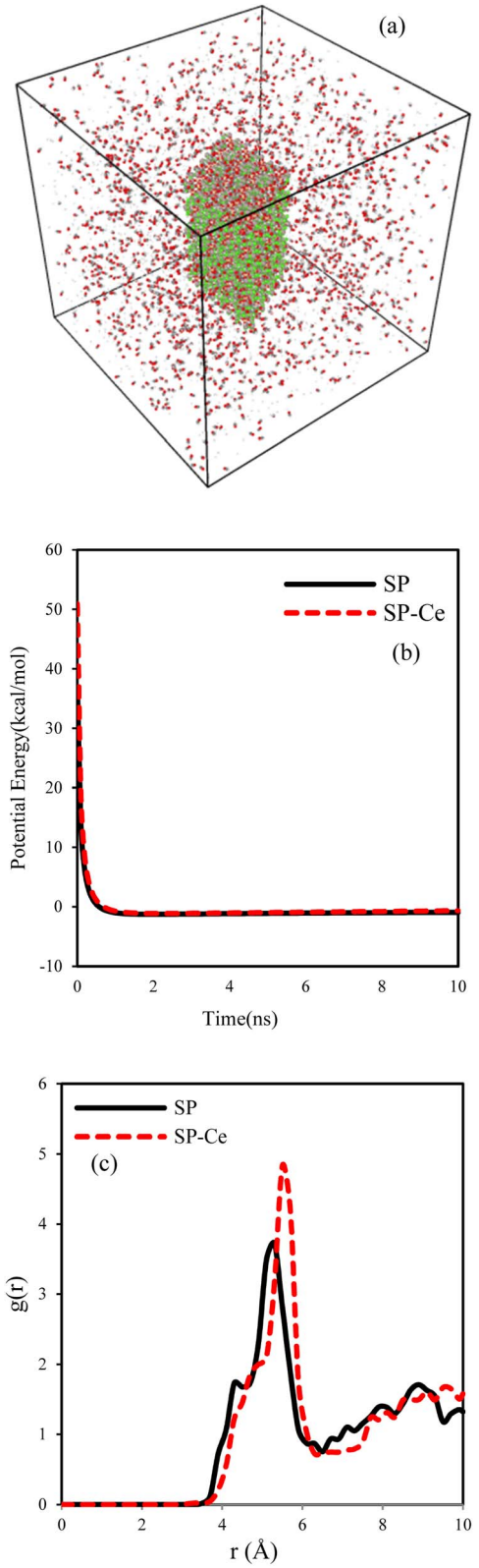

Fig. 1 (a) Initial atomic arrangement in MD simulations, (b) Potential energy profiles of SP and SP-Ce structures during equilibrium at 300 K and 1 atm (initial conditions), and (c) RDF profiles of both structures at equilibrium after 10 ns.

analysis. From the equilibrated geometries, static energy calculations are then conducted to determine the energies of the reactant and product states. Based on these values, the forward (E_f) and reverse (E_r) reaction energies, as well as the overall energy change (ΔE), are estimated from the differences between the initial and final states. We emphasize that the MD simulations are not used to directly identify transition states or compute activation barriers; rather, they serve to generate thermally equilibrated structures for subsequent static energy evaluation. This distinction clarifies the methodology and avoids the misconception that plain MD trajectories are sufficient for barrier calculations without additional sampling or optimization techniques.

The correctness of the defined atomic structures—including simulation box dimensions ($350 \times 350 \times 350$ Å^3), atomic arrangement, and boundary conditions—together with simulation settings such as the chosen force field, time step, and membrane geometry, is validated through potential energy convergence analysis under the specified initial conditions. This relatively large simulation box size is required to accommodate a realistic SAPO-34 supercell with CeO_2 dopants and to prevent spurious interactions between periodic images. The modeled system contains all atoms and employs periodic boundary conditions in all three dimensions. Each system was first relaxed in the NVT ensemble for 2 ns, followed by 3 ns in the NPT ensemble to stabilize pressure and density. The subsequent 10 ns production run was carried out with a 1 fs timestep.

The potential energy profiles of two representative systems (SP and SP-Ce) are shown in Fig. 1b. In both cases, the potential energy converges within 10 ns to -0.94 kcal mol^{-1} (SP) and -0.68 kcal mol^{-1} (SP-Ce), indicating stable atomic interactions. As the simulation progresses, atomic fluctuation amplitudes decrease, reflecting the attainment of structural and thermodynamic equilibrium. The radial distribution function (RDF), shown in Fig. 1c, further confirms equilibration: distinct RDF peaks indicate stable atomic coordination distances within the simulation cell. Together, the potential energy and RDF analyses verify that 10 ns is sufficient to achieve equilibrium under the chosen simulation conditions.

To address the temperature dependence of catalytic properties, we plan to perform additional MD simulations at 698 K for selected systems, enabling a comparison of structural stability, RDF features, and potential energy trends between ambient and operating temperatures. This will allow us to assess whether temperature scaling or entropic effects significantly influence the equilibrated structures used for subsequent energy calculations.[34,35]

2.4. MTO catalytic tests

The MTO process is conducted in a fixed-bed reactor under atmospheric pressure and at a reaction temperature of 425 °C. Prior to each experimental run, 2 g of the calcined catalyst (sized to 40–20 mesh) are mixed with 4 g of inert silicon carbide (SiC)

and loaded into the reactor. To prepare the catalyst for reaction, it undergoes a pretreatment step at 550 °C for 1 h under a continuous flow of nitrogen. This step (Fig. 2) ensures the removal of moisture and any residual contaminants, thereby enhancing the catalyst's activity and stability. Once the catalyst is pretreated, the reactor is allowed to cool down to the desired reaction temperature. At this point, a methanol–water feed mixture, with a weight ratio of 72 : 28, is introduced into the system. The feed is supplied at a weight hourly space velocity (WHSV) of 2 h^{-1}, ensuring optimal contact between the reactants and the catalyst.[36]

The reaction products are continuously analyzed using an Agilent GC 7890A gas chromatograph equipped with both flame ionization detectors (FID) and thermal conductivity detectors (TCD). This dual detection system provides precise quantification of hydrocarbon products and non-hydrocarbon gases, offering a comprehensive profile of the reaction output. These analytical capabilities enable the detailed monitoring of product distribution and catalytic performance throughout the MTO reaction.

3. Results and discussion

3.1. Characterization analyses

3.1.1. Crystalline and structural properties. The XRD patterns of the SP and SP-Ce samples are depicted in Fig. 3a. Both samples display prominent diffraction peaks at 2θ values near 9.6°, 20.7°, 26°, and 31°, which are indicative of the CHA (chabazite) framework. These peaks confirm that the crystalline structure of SAPO-34 is preserved in both samples. The crystalline phase in SP and SP-Ce corresponds to a hexagonal prism geometry, as validated by the JCPDS standard card 01-087-1527.[37,38]

The diffraction peak intensities of SP are higher than those of SP-Ce, reflecting greater crystallinity in the undoped SAPO-34 sample. The reduced peak intensity in SP-Ce is attributed to the incorporation of cerium oxide (CeO_2) into the SAPO-34 framework. The doping process introduces lattice distortions and slightly disrupts the long-range crystalline order, a common effect observed in modified SAPO materials.

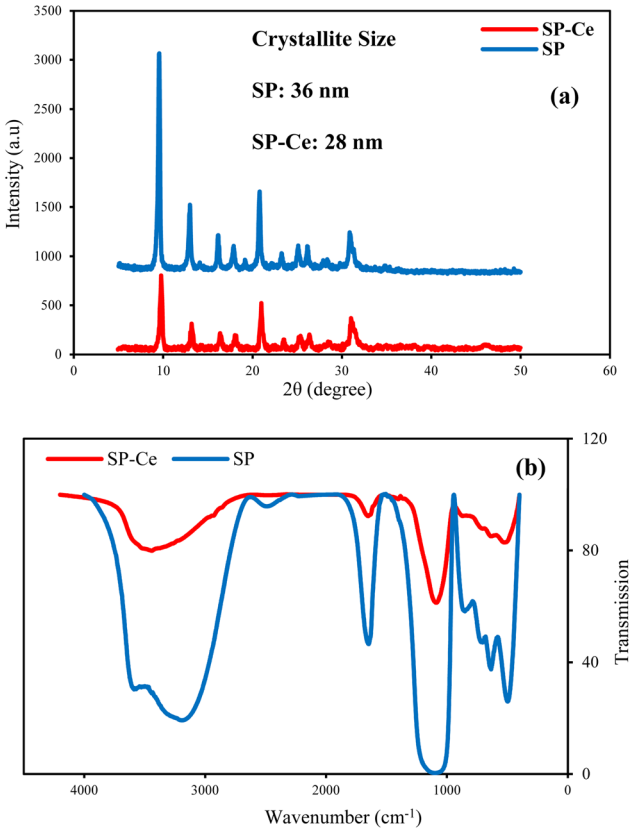

Fig. 3 (a) XRD profiles of SP and SP-Ce along with their crystallite sizes. (b) Their FT-IR spectra.

Crystallite size calculations using the Scherrer equation indicate that SP has a crystallite size of approximately 36 nm, while SP-Ce exhibits a smaller size of around 31 nm. This reduction in crystallite size upon ceria incorporation suggests structural changes within the lattice and a decrease in crystalline domain size. Such a reduction is advantageous for catalytic

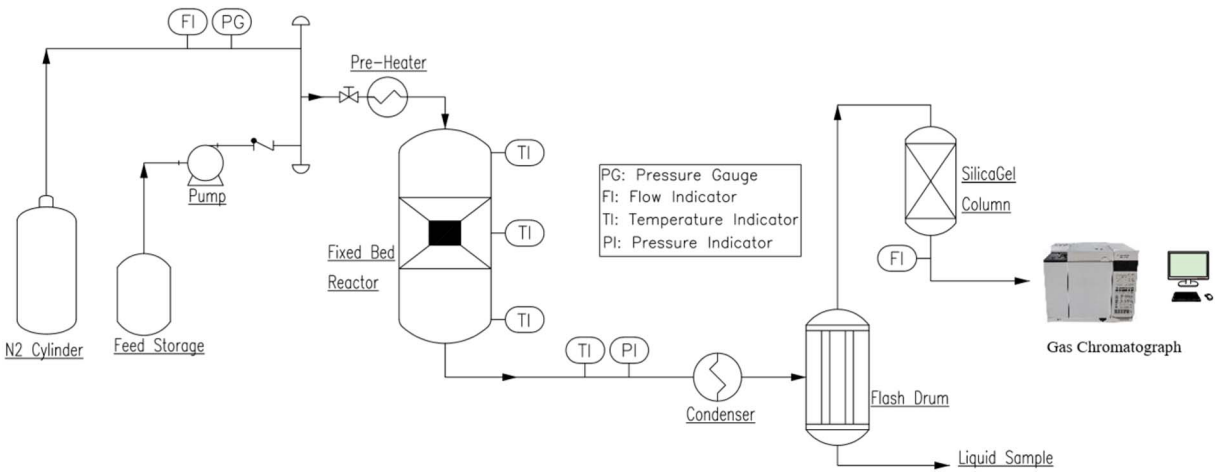

Fig. 2 Process flow diagram of MTO catalytic performance experimental setup.

applications, as smaller crystallites increase surface area and enhance access to active sites, potentially improving the catalytic efficiency in the MTO process.[38] Moreover, the absence of secondary peaks associated with crystalline CeO_2 in the XRD pattern of SP-Ce indicates that cerium species are highly dispersed within the SAPO-34 framework. This suggests that cerium oxide is effectively integrated into the SAPO-34 matrix without significant phase separation or aggregation.[37–40]

The FT-IR spectra of SP and SP-Ce, exhibited in Fig. 3b, highlight the vibrational characteristics of functional groups in the SAPO-34 framework and the effects of cerium oxide incorporation. Both spectra display distinct absorption bands typical of SAPO-34, confirming the retention of its structural framework after cerium doping. The characteristic bands observed between 1000 and 1250 cm^{-1} correspond to the asymmetric stretching vibrations of T–O–T (T = Si, Al, or P) linkages, while bands around 750–800 cm^{-1} are attributed to symmetric stretching vibrations of the same linkages. Peaks below 600 cm^{-1} are associated with bending vibrations. These vibrations remain consistent in both SP and SP-Ce, indicating that the fundamental chabazite structure of SAPO-34 is preserved after CeO_2 incorporation.[41–43]

A broad band centered at 3400–3600 cm^{-1} is observed in both samples, corresponding to O–H stretching vibrations associated with surface hydroxyl groups and adsorbed water. This band is slightly less intense in SP-Ce, suggesting that cerium doping reduces water adsorption or modifies hydroxyl groups. Additionally, the bending vibration of adsorbed water is detected near 1630 cm^{-1} in both samples, confirming the presence of moisture. Notable shifts and changes in the intensity of certain peaks, such as those near 1100 cm^{-1} and 800 cm^{-1} in SP-Ce, point to interactions between cerium species and the SAPO-34 framework. These shifts are likely due to changes in bond angles or lengths caused by cerium incorporation. Importantly, no additional peaks corresponding to crystalline ceria are observed, indicating that cerium species are highly dispersed and effectively integrated into the SAPO-34 matrix without forming separate phases.[37,40,44–46]

The FT-IR analysis provides conclusive evidence that the SAPO-34 framework remains intact after ceria incorporation, with minor structural modifications. The preservation of key T–O–T vibrations demonstrates the stability of the chabazite structure, while the reduced intensity of O–H vibrations suggests alterations in surface properties, potentially improving catalytic performance by reducing moisture adsorption and modifying acid site distribution.[43]

3.1.2. Morphology and chemical composition. The FESEM images of SP and SP-Ce reveal significant morphological differences, reflecting the impact of cerium oxide incorporation on the SAPO-34 framework (Fig. 4). SP exhibits well-defined cubic crystals with smooth surfaces and uniform geometry, characteristic of high crystallinity and minimal structural defects.[47] The average particle size of SP is 1.7 μm, as presented in Table 1, indicating successful synthesis with proper nucleation and growth during the crystallization process.

In contrast, SP-Ce demonstrates smaller particles with irregular shapes and rough surfaces, with an average particle size reduced to 1.05 μm. The cubic morphology observed in SP is less pronounced in SP-Ce, with particles appearing fragmented or clustered. This morphological alteration is attributed to CeO_2 doping, which disrupts the uniform crystal growth by altering nucleation and growth kinetics during synthesis. The rougher surface and irregular morphology of SP-Ce suggest lattice distortions and structural irregularities, likely caused by interactions between CeO_2 and the SAPO-34 framework, consistent with findings from other reports.[48,49] The smaller particle size and rougher surface of SP-Ce align with XRD results, which indicate a reduction in crystallite size from 36 nm (SP) to 31 nm (SP-Ce). These structural modifications enhance SP-Ce's surface area and accessibility to active sites, offering potential advantages for catalytic applications, particularly in MTO reactions.[50]

The elemental composition and silicon incorporation provide further insights into the structural and chemical changes induced by CeO_2 doping, as listed in Table 1. In SP, the mole composition of $Al_{0.735}P_{0.244}Si_{0.144}O_2$ corresponds to a Si/(Si + Al + P)$_{solid}$ ratio of 0.129, closely matching the gel ratio of 0.13. This indicates efficient silicon incorporation during synthesis, with an incorporation efficiency of 0.988. The Si/Al ratio of 0.196 reflects a balanced distribution of silicon and aluminum,

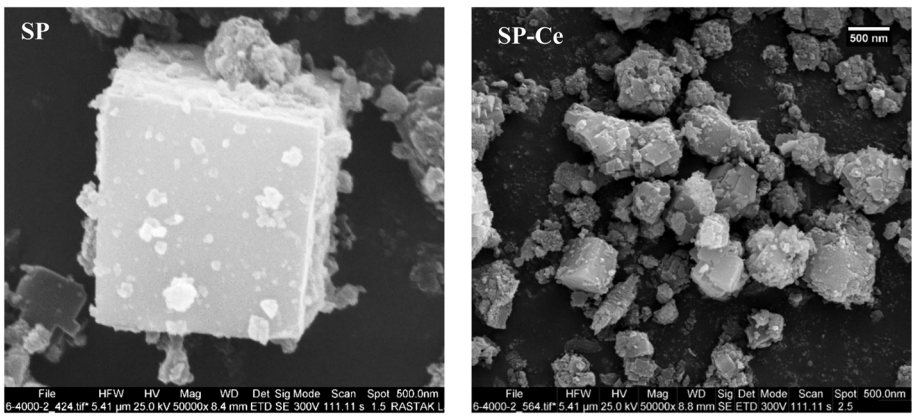

Fig. 4 The FESEM images of both SAPO-34 (SP and SP-Ce).

Table 1 Elemental composition of both SAPO-34 (SP and SP-Ce) and their average particles size

Samples	Mole composition	$Si/(Si + Al + P)_{solid}$	$Si/(Si + Al + P)_{gel}$	Si incorporation	Si/Al	Ce (wt%)	Particle size (μm)
SP	$Al_{0.735}P_{0.244}Si_{0.144}O_2$	0.129	0.13	0.988	0.196	—	1.7
SP-Ce	$Al_{0.658}P_{0.338}Si_{0.087}O_2$	0.076	0.13	0.596	0.127	4.1	1.05

contributing to SP's microporous structure and catalytic activity.

In SP-Ce, the mole composition of $Al_{0.658}P_{0.338}Si_{0.084}O_2$ reveals a decrease in the $Si/(Si + Al + P)_{solid}$ ratio to 0.077, while the gel ratio remains at 0.13. This results in a reduced silicon incorporation efficiency of 0.596 and a lower Si/Al ratio of 0.127. The reduction in silicon incorporation and Si/Al ratio suggests that cerium interacts competitively with silicon during synthesis, hindering its integration into the framework. Additionally, SP-Ce shows an increase in phosphorus content, reflecting a redistribution of elements likely influenced by cerium's presence.

The Ce 3d high-resolution spectra (Fig. 5) show the characteristic peaks of Ce $3d_{5/2}$ and Ce $3d_{3/2}$, confirming the presence of ceria species on the SP-Ce catalyst surface. Deconvolution of the spectra reveals two oxidation states: Ce^{4+}, represented by five peaks, and Ce^{3+}, represented by two peaks. The coexistence of Ce^{3+} and Ce^{4+} in CeO_{2-X} indicates the presence of oxygen vacancies ($X > 0$), which are known to enhance catalytic performance by suppressing carbon deposition and delaying catalyst deactivation.[51,52] These oxygen vacancies also modulate the redox and acid–base properties of the catalyst, thereby improving its resistance to coke formation during the MTO process.[53] Complementary EDS analysis confirms a cerium content of 4.1 wt% in SP-Ce, demonstrating successful incorporation of Ce species into the SAPO-34 framework or surface. Together with the XRD and FT-IR evidence of high Ce dispersion, these results suggest that Ce species are well-distributed within the catalyst, where their mixed oxidation states and associated oxygen vacancies play a key role in enhancing stability and performance.

The changes in elemental composition and morphology caused by CeO_2 doping have significant implications for the material's structural and catalytic properties. The reduced Si/Al ratio in SP-Ce may lower the material's acidity, which is critical for catalytic activity. However, the introduction of cerium compensates by introducing redox-active sites, enhancing the material's potential for redox-based catalytic applications. Furthermore, the increased mesoporosity and rougher particle surfaces improve molecular diffusion and accessibility to active sites, optimizing SP-Ce for reactions involving bulky molecules.[54]

The structural irregularities and rough morphology of SP-Ce, along with its smaller particle and crystallite sizes, result in a hierarchical microporous–mesoporous framework. This dual porosity, combined with the altered elemental composition, significantly enhances the material's performance in catalytic and adsorption applications requiring efficient mass transfer and reactivity. CeO_2 doping profoundly impacts SAPO-34 by transforming its well-defined cubic crystals (SP) into irregular, rough particles (SP-Ce) and altering silicon incorporation and the Si/Al ratio. These changes introduce mesoporosity, redox-active sites, and improved accessibility to active regions, making SP-Ce a promising candidate for the MTO process.[50]

3.1.3. Textural properties. The nitrogen adsorption–desorption isotherms of SP and SP-Ce exhibit type-IV characteristics, indicative of mesoporous materials (Fig. 6). The hysteresis loops, observed at relative pressures (P/P_0) of 0.45 for SP and 0.31 for SP-Ce, confirm the presence of mesopores in both materials.[55,56] The earlier onset of the hysteresis loop in SP-Ce reflects structural alterations caused by CeO_2 doping, which increases the fraction of mesopores and enhances overall porosity.

The surface areas and pore volumes of both samples are presented in Table 2. The BET surface area (S_{BET}) of SP is 344.0 $m^2\ g^{-1}$, which decreases to 288.7 $m^2\ g^{-1}$ for SP-Ce due to CeO_2 doping. This reduction suggests that CeO_2 partially blocks micropores and covers the surface of SAPO-34. Correspondingly, the external surface area (S_{ext}) decreases from 81.4 $m^2\ g^{-1}$ for SP to 53.5 $m^2\ g^{-1}$ for SP-Ce. Similarly, the micropore surface area (S_{micro}) drops from 262.6 $m^2\ g^{-1}$ to 235.2 $m^2\ g^{-1}$, indicating a reduction in microporosity.

In contrast, mesoporosity increases significantly upon doping. The mesopore volume (V_{meso}) rises from 0.060 $cm^3\ g^{-1}$ for SP to 0.150 $cm^3\ g^{-1}$ for SP-Ce, while the total pore volume (V_{total}) increases from 0.164 $cm^3\ g^{-1}$ to 0.302 $cm^3\ g^{-1}$. These changes highlight the creation of mesopores and the overall enhancement in pore accessibility. The pore size distribution analysis further supports this, showing that SP primarily exhibits microporous characteristics with a sharp peak below 2 nm, whereas SP-Ce displays a broader distribution extending into the mesoporous range of 2–50 nm.

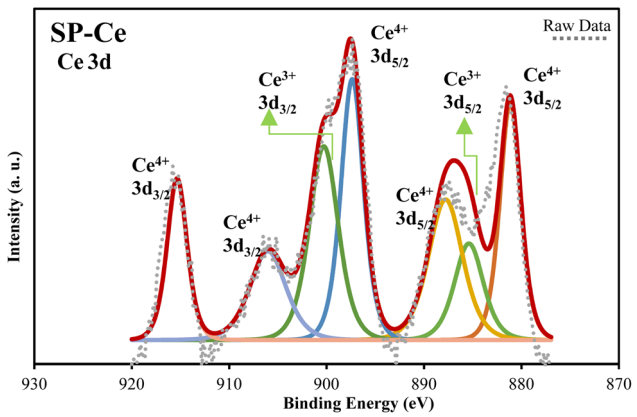

Fig. 5 The HR-XPS spectra of Ce 3d for SP-Ce catalyst.

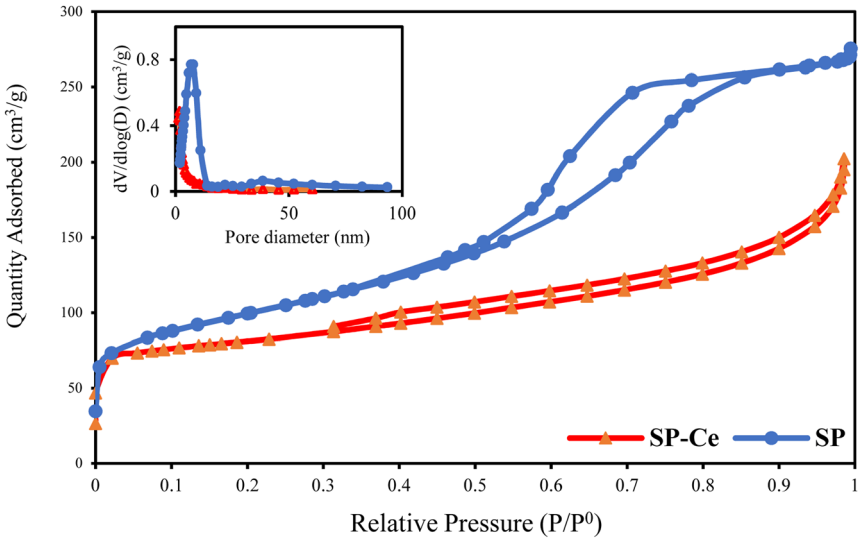

Fig. 6 N_2-adsorption/desorption isotherm and BJH adsorption cumulative pore volume of SP and SP-Ce samples.

Table 2 Physical properties of SP and SP-Ce samples

	Surface area ($m^2\ g^{-1}$)			Pore volume ($cm^3\ g^{-1}$)		
Samples	S_{BET}	S_{ext}	S_{micro}	V_{micro}	V_{meso}	V_{total}
SP	344.0	81.4	262.6	0.104	0.060	0.164
SP-Ce	288.7	53.5	235.2	0.152	0.150	0.302

The structural modifications induced by CeO_2 doping are reflected in the hysteresis behavior, where the lower onset of the loop in SP-Ce aligns with its increased mesoporosity and total pore volume. CeO_2 doping transforms SAPO-34 from a predominantly microporous material to a hierarchical microporous–mesoporous structure. This modification, characterized by increased mesopore volume, broader pore size distribution, and a shift in hysteresis behavior, balances surface area and pore accessibility, optimizing the material for specific catalytic and adsorption applications. The enhanced mesoporosity facilitates the diffusion of bulky molecules, potentially improving catalytic performance in reactions involving larger substrates.[57] However, the reduction in microporous surface area and BET surface area may slightly diminish the material's adsorption capacity for smaller molecules.[24]

3.1.4. Acidity. The NH_3-TPD profiles of SP and SP-Ce, depicted in Fig. 7, along with FT-IR analysis, reveal significant differences in acidity and surface chemistry, highlighting the impact of CeO_2 doping on the SAPO-34 framework. These changes are evident in the number, strength, and distribution of acid sites, as well as modifications to surface hydroxyl groups.

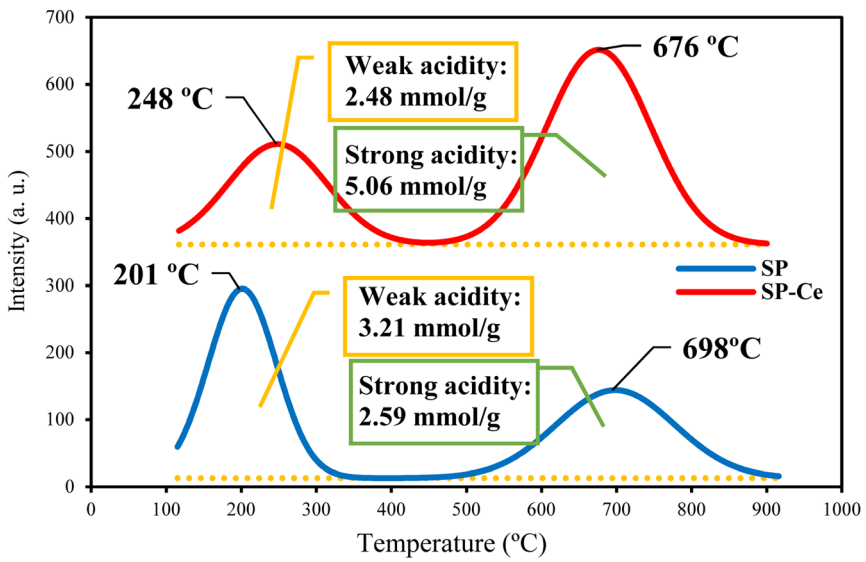

Fig. 7 NH_3-TPD profiles of SP and SP-Ce samples.

In SP, the NH_3-TPD profiles exhibit desorption peaks at 201 °C and 698 °C, corresponding to weak and strong acid sites, respectively. The weak acidity is measured at 3.21 mmol g^{-1}, while the strong acidity is 2.59 mmol g^{-1}. The weak acid sites are associated with hydroxyl (OH) groups attached to defect sites such as POH, SiOH, and AlOH. In contrast, the strong acid sites are attributed to hydroxyl groups of (Si–OH–Al) bridges located inside the zeolite channels, which serve as critical structural acidic centers. These strong acid sites are essential for the MTO process, as they facilitate the conversion of methanol to light olefins.[40,44,58]

CeO_2 doping in SP-Ce significantly modifies the acidity profile. The desorption temperatures for weak and strong acid sites shift to 248 °C and 676 °C, respectively, reflecting changes in acid strength and distribution. While the weak acid sites exhibit a moderate increase in strength (higher desorption temperature), their overall concentration decreases compared to SP. On the other hand, the strong acid site concentration nearly doubles to 5.06 mmol g^{-1} after CeO_2 incorporation, accompanied by a slight decrease in desorption temperature, which suggests a mild weakening in average acid strength. The observed increase is therefore more reasonably attributed to the formation of new Lewis acid centers associated with Ce^{3+}/Ce^{4+} species and oxygen vacancies. These Ce-induced Lewis acid sites, in synergy with the intrinsic Brønsted acidity of the SAPO-34 framework, create a more balanced acidity profile that improves methanol activation, enhances light olefin selectivity, and increases resistance against coke deposition, thereby significantly boosting the catalytic efficiency of SP-Ce.

Weak acid sites play a supportive role in the MTO process by facilitating the initial conversion of methanol to methoxy intermediate species and subsequently to dimethyl ether (DME). Although they do not directly contribute to the production of light olefins, they are essential in enabling the reaction pathway by forming the necessary intermediates. The FT-IR analysis reveals that CeO_2 doping alters the distribution of surface hydroxyl groups, particularly influencing weak acid sites. The reduction in weak acid sites in SP-Ce moderates the conversion of methanol to methoxy intermediate species and diminishes their accumulation on the SAPO-34 surface. This moderation reduces the likelihood of forming formaldehyde species, known precursors to coke formation, which can enhance the durability of the catalyst during the MTO process.[43,59]

Strong acid sites remain the key active centers for converting DME to light olefins in the MTO process. The significant increase in strong acid sites in SP-Ce, coupled with their redistribution, ensures more efficient conversion of DME to olefins. This modification in the acidity properties of SP-Ce promises enhanced activity due to the complementary roles of moderately weak and strongly boosted acid sites: the moderately weak acid sites prepare an appropriate percentage of intermediates, while the strong acid sites effectively drive the critical steps of olefin production. The NH_3-TPD underscore the profound impact of CeO_2 doping on the acidity of SAPO-34. CeO_2 not only alters the distribution and strength of acid sites but also enhances the concentration of strong acid sites and optimizes the role of weak acid sites in the reaction pathway, aligning with other reports.[60,61]

3.1.5. Mechanistic insights using MD simulations. The MD simulations provide atomistic insights into the reaction pathways of SP and SP-Ce catalysts in the MTO process, with particular focus on energy barriers governing coke formation and consumption. The calculated parameters include the forward activation energy (E_f), reverse activation energy (E_r), and overall energy difference (ΔE), which together describe the kinetics and thermodynamics of elementary steps (R1)–(R6) (Fig. 8). These reactions involve the generation and transformation of surface-bound intermediates that strongly influence catalyst stability and product selectivity.[5–7,11,62,63]

Reactions (R1)–(R3) represent the primary routes for the formation of surface-bound formyl species (–CHO, denoted as CHO-θ), which are key precursors to coke deposition. (R1) corresponds to the thermal decomposition of methoxy groups (CH_3O-θ) to yield CHO-θ and water. (R2) describes a hydride transfer between methoxy and ethylene, producing CHO-θ alongside ethane. (R3) involves methanol disproportionation, generating CHO-θ and surface hydrogen species. Together, these pathways demonstrate how CHO-θ intermediates form on Lewis acid sites, initiating coke nucleation and subsequent catalyst deactivation.

$$2CH_3O\text{-}\theta + \theta \leftrightarrow CHO\text{-}\theta + CH_3\text{-}\theta + H_2O\text{-}\theta \quad (R1)$$

$$CH_3O\text{-}\theta + C_2H_4\text{-}2\theta \leftrightarrow CHO\text{-}\theta + C_2H_6\text{-}2\theta \quad (R2)$$

$$CH_3O\text{-}\theta + 2\theta \leftrightarrow CHO\text{-}\theta + 2H\text{-}\theta \quad (R3)$$

Subsequent transformations ((R4)–(R6)) highlight how these intermediates evolve into gaseous products or coke precursors. (R4) describes further decomposition of CHO-θ into CO-θ and H-θ. (R5) represents the water–gas shift-like step, converting CO-θ and H_2O-θ into CO_2-θ and H_2-θ. Finally, (R6) captures CO_2

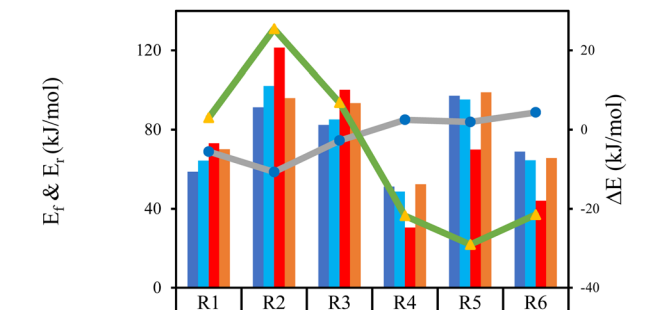

	R1	R2	R3	R4	R5	R6
Ef (SP)	58.64	91.28	82.35	51.03	97.09	68.76
Er (SP)	64.22	102.02	85.13	48.55	95.15	64.42
Ef (SP-Ce)	73.01	121.3	100.16	30.51	69.83	44.08
Er (SP-Ce)	69.99	95.84	93.34	52.26	98.88	65.55
ΔE (SP)	-5.58	-10.74	-2.78	2.48	1.94	4.34
ΔE (SP-Ce)	3.02	25.46	6.82	-21.75	-29.05	-21.47

Fig. 8 Energy barriers and differences for six key reactions ((R1)–(R6)) over both SAPO-34 (SP and SP-Ce).

reduction with surface carbon species to form two CO-θ units, potentially feeding back into coke-related pathways.

$$\text{CHO-}\theta + \theta \leftrightarrow \text{CO-}\theta + \text{H-}\theta \quad \text{(R4)}$$

$$\text{CO-}\theta + \text{H}_2\text{O-}\theta \leftrightarrow \text{CO}_2\text{-}\theta + \text{H}_2\text{-}\theta \quad \text{(R5)}$$

$$\text{CO}_2\text{-}\theta + \text{C-}\theta \leftrightarrow 2\text{CO-}\theta \quad \text{(R6)}$$

The relative magnitudes of E_f and E_r can provide a mechanistic explanation for the experimentally observed trends in selectivity and stability.[64] The E_f of (R1) increases significantly from 58.64 kJ mol^{-1} for SP to 73.01 kJ mol^{-1} for SP-Ce, indicating a higher resistance to the thermal decomposition of methanol in the doped catalyst. The E_r of (R1) for SP-Ce is slightly reduced (69.99 kJ mol^{-1}) compared to SP (64.22 kJ mol^{-1}), resulting in a shift in thermodynamic favorability. The ΔE of (R1) for SP-Ce is positive (3.02 kJ mol^{-1}), indicating an endothermic nature, while SP shows a slightly exothermic reaction (−5.58 kJ mol^{-1}). Fig. 8 shows that (R2) illustrates a sharp increase in E_f from 91.28 kJ mol^{-1} (SP) to 121.3 kJ mol^{-1} (SP-Ce), reflecting a higher energy barrier for CHO-θ formation in SP-Ce. Besides, the E_r of (R2) for SP-Ce decreases to 95.84 kJ mol^{-1} compared to SP (102.02 kJ mol^{-1}). A substantial change in ΔE of (R2) is observed, shifting from −10.74 kJ mol^{-1} in SP to 25.46 kJ mol^{-1} in SP-Ce, indicating that CeO_2 doping makes this reaction less favorable thermodynamically. E_f of (R3) increases from 82.35 kJ mol^{-1} (SP) to 100.16 kJ mol^{-1} (SP-Ce), indicating a slower disproportionation process for the doped catalyst. E_r of (R3) also rises in SP-Ce (93.34 kJ mol^{-1}) compared to SP (85.13 kJ mol^{-1}). The ΔE of (R3) remains slightly endothermic for SP-Ce (6.82 kJ mol^{-1}) compared to the nearly thermoneutral ΔE of −2.78 kJ mol^{-1} in SP.

In addition to reactions that generate CHO-θ, (R4) is included to explore a potential pathway for suppressing CHO-θ accumulation. This reaction converts CHO-θ into less harmful intermediates such as CO and H, reducing the likelihood of coke formation and enhancing catalyst durability. The kinetic feasibility of this suppression pathway is evaluated by comparing the forward and reverse energy barriers (E_f and E_r), which indicate the effectiveness of the catalyst in mitigating CHO-θ accumulation. (R4) demonstrates a significant reduction in E_f for SP-Ce (30.51 kJ mol^{-1}) compared to SP (51.03 kJ mol^{-1}), indicating improved efficiency in suppressing CHO-θ accumulation. However, the reverse barrier increases from 48.55 kJ mol^{-1} (SP) to 52.26 kJ mol^{-1} (SP-Ce). Importantly, ΔE of (R4) becomes highly exothermic (−21.75 kJ mol^{-1}) in SP-Ce, compared to 2.48 kJ mol^{-1} in SP, showing that CeO_2 doping makes this reaction thermodynamically favorable and kinetically accessible.

Reactions (R5) and (R6) focus on mechanisms for coke removal. (R5) represents the water-gas shift reaction, which generates activated CO_2 by converting CO and water into CO_2 and H_2. The activated CO_2 then plays a critical role in (R6), the reverse Boudouard reaction, which oxidizes deposited carbon on the catalyst surface to CO. Together, these reactions provide a means of regenerating the catalyst by consuming deposited coke, thereby enhancing its durability. By studying these reactions, the ability of the catalyst to actively manage coke formation and removal is assessed. E_f of (R5) for SP-Ce is significantly lower (69.83 kJ mol^{-1}) than SP (97.09 kJ mol^{-1}), suggesting enhanced progression of WGS in the doped catalyst. E_r of (R5) is slightly higher for SP-Ce (98.88 kJ mol^{-1}) compared to SP (95.15 kJ mol^{-1}). ΔE shifts from a slightly endothermic 1.94 kJ mol^{-1} in SP to a highly exothermic −29.05 kJ mol^{-1} in SP-Ce, indicating greater thermodynamic favorability for SP-Ce to CO_2 formation through accomplishing WGS reaction. E_f of (R6) decreases significantly in SP-Ce (44.08 kJ mol^{-1}) compared to SP (68.76 kJ mol^{-1}), reflecting enhanced coke consumption in the doped catalyst. E_r of (R6) for SP-Ce increases slightly to 65.55 kJ mol^{-1} compared to SP (64.42 kJ mol^{-1}). ΔE of (R6) becomes strongly exothermic (−21.47 kJ mol^{-1}) for SP-Ce, compared to a weakly endothermic 4.34 kJ mol^{-1} in SP, indicating greater efficiency in carbon removal.

While SP contains Lewis acid sites essential for facilitating the MTO process, these same sites are prone to promoting coke formation through CHO-θ intermediates, a critical precursor to carbonaceous deposits that deactivate the catalyst. Doping SAPO-34 with CeO_2 introduces redox-active sites, which are expected to significantly influence key reactions involved in coke management. Specifically, these sites enhance CO_2 formation and activation, improving the efficiency of coke removal pathways such as the water–gas shift (R5) and the Boudouard reaction (R6). This modification is anticipated to result in superior performance in terms of catalyst durability and selectivity to olefins by reducing coke formation and promoting its removal. Furthermore, by maintaining active catalytic sites through efficient suppression and removal of coke, the SP-Ce catalyst is expected to sustain higher olefin selectivity during the MTO process.

3.1.6. MTO catalytic tests. The catalytic performance of SP and SP-Ce for the MTO process was investigated in a fixed-bed reactor at atmospheric pressure, 425 °C, with a WHSV of 2 h^{-1} and a methanol feed composition of 72 wt% in water. Fig. 9a shows the total olefin selectivity as a function of time on stream (TOS) for both catalysts. The SP catalyst initially achieves a selectivity of 31.4% at 60 min, peaking at 76.6% after 240 min. However, a noticeable deactivation occurs after 420 min, with selectivity declining to 41.4%. In contrast, SP-Ce demonstrates superior performance, with an initial selectivity of 53%, peaking at 83.9% at 420 min and maintaining 54.9% selectivity at 600 min. This enhanced stability is attributed to the incorporation of CeO_2, which reduces coke formation and preserves active sites.

Fig. 9b presents the selectivity distribution for light olefins, ethylene (C_2=), propylene (C_3=), and butene (C_4=). SP shows ethylene, propylene, and butene selectivities of 35.51%, 38.33%, and 2.75%, respectively. SP-Ce achieves improved propylene selectivity (41.47%) while maintaining similar ethylene selectivity (39.79%) and low butene selectivity (2.64%). CeO_2 doping modifies the acid site distribution, enhancing the propylene-to-ethylene ratio and favoring ethylene production, which is in good agreement with other studies.[65,66]

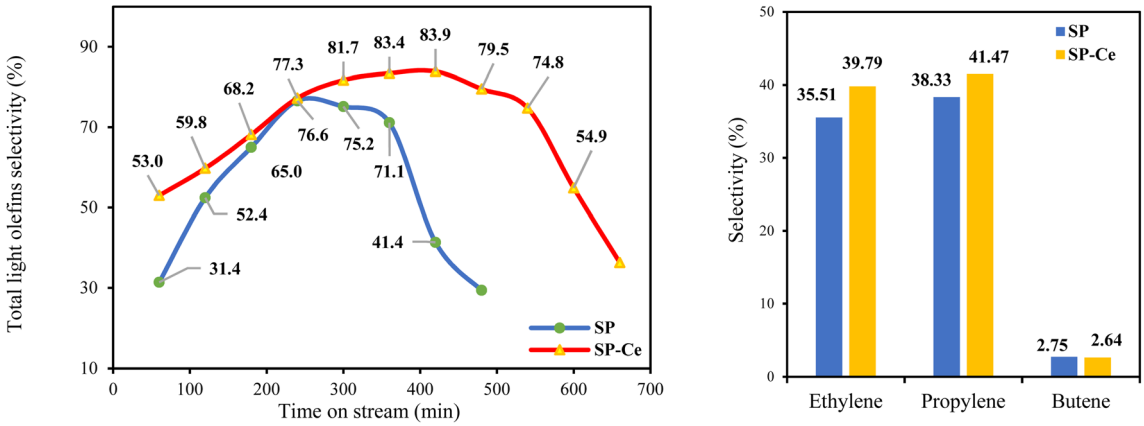

Fig. 9 (a) Selectivity of light olefins and (b) product distribution (C_2=–C_4=) for SP and SP-Ce samples under specified test conditions (T = 425 °C, catalyst weight = 2 g, WHSV = 2 h^{-1}).

In addition, coke formation plays a decisive role in determining the stability, catalytic activity, and overall lifetime of SAPO-34 in the MTO process. Both the total amount of coke deposited and the rate of coke accumulation (R_{Coke}) are key indicators of deactivation behavior. Thermogravimetric analysis of the spent samples (Table 3) shows comparable total coke contents for the two catalysts, with values of 9.7% (g g_{cat}^{-1}) for SP and 10.1% (g g_{cat}^{-1}) for SP-Ce. The difference becomes evident, however, in the coke deposition rate: SP reaches 0.20 mg g_{cat}^{-1} min^{-1}, while SP-Ce is lower at 0.15 mg g_{cat}^{-1} min^{-1}. This reduced coke accumulation rate correlates with the enhanced stability of SP-Ce, which maintains activity for 660 minutes on stream, compared with only 480 minutes for SP before pronounced deactivation occurs.

The superior catalytic performance of SP-Ce compared to the SP in the MTO process is strongly tied to its structural, textural, and chemical properties, as revealed by characterization and MD simulations. SP exhibits a crystallite size of ~36 nm with a uniform cubic morphology. However, its microporous structure limits mass transfer, and the absence of mesoporosity leads to rapid deactivation due to coke accumulation.[67] CeO_2 doping reduces the crystallite size to ~31 nm and transforms the cubic crystals into irregular, rough particles, introducing a hierarchical microporous–mesoporous framework. This enhances mass transfer, increases pore volume, and facilitates the diffusion of bulky intermediates, mitigating pore blockage and improving catalytic efficiency. The mesoporosity of SP-Ce, confirmed by hysteresis behavior, combined with smaller particle sizes, increases surface area availability, contributing to higher olefin selectivity and prolonged stability.[68]

Acidity plays a pivotal role in the MTO reaction, and the two catalysts exhibit distinct acid site distributions. SP contains a high concentration of weak acid sites, which promote methoxy intermediate accumulation and increase coke formation. CeO_2 doping optimizes SAPO-34's acidity by reducing weak acid sites and redistributing strong acid sites. Strong acid sites efficiently drive olefin production, while moderated weak acid sites reduce formaldehyde formation, a precursor to coke. NH_3-TPD and FT-IR analyses confirm this balanced acidity, ensuring efficient methanol conversion and reduced coking tendencies.

Mechanistic insights from MD simulations reveal that CeO_2 suppresses the formation of CHO-θ intermediates, which are key precursors to coke, and enhances coke removal through improved CO_2 activation and the Boudouard reaction. The redistribution of acid sites in SP-Ce balances intermediate preparation (*via* weak acid sites) and olefin production (*via* strong acid sites), further improving methanol conversion pathways.

The synergy between experimental results, characterization data, and MD simulations underscores the transformative role of CeO_2 doping. SP's larger crystallite size, lack of mesoporosity, and excessive weak acid sites contribute to rapid deactivation due to limited mass transfer and coke formation. Conversely, CeO_2-doped SP-Ce exhibits smaller crystallite size, hierarchical mesoporosity, and optimized acidity, enhancing mass transfer, reducing coking, and sustaining olefin production, particularly ethylene. These dual benefits, structural improvements (enhanced mesoporosity and particle size reduction) and functional enhancements (optimized acidity and coking resistance), position SP-Ce as a superior catalyst for the MTO process. CeO_2 incorporation significantly prolongs catalyst life, enhances olefin selectivity, particularly ethylene, and improves operational stability, making SP-Ce a highly promising catalyst for industrial applications.

Table 3 Coke content and coke deposition rate over all samples

Samples	TOS (min)	Coke capacity (%, g g_{cat}^{-1})	R_{Coke} (mg g_{cat}^{-1} min^{-1})
SP	480	9.7	0.20
SP-Ce	660	10.1	0.15

4. Conclusion

The incorporation of cerium oxide into SAPO-34 provides groundbreaking mechanistic insights that drive its enhanced performance in the MTO process. MD simulations highlight the suppression of coke-forming CHO-θ intermediates and the promotion of efficient coke removal *via* CO_2 activation and the Boudouard reaction, mechanisms critical to sustaining catalytic activity and selectivity. Complementary experimental findings reveal that CeO_2 reduces the crystallite size from ~36 nm to ~31 nm and transforms SAPO-34 from a microporous structure to a hierarchical microporous–mesoporous framework. These structural changes facilitate mass transfer, increase pore accessibility, and enhance the diffusion of bulky intermediates, mitigating pore blockage.

CeO_2 doping also introduces a novel redistribution of acid sites, balancing weak and strong acid sites to optimize methanol conversion pathways. The reduction of weak acid sites minimizes coke precursors, while enhanced strong acid sites drive olefin production. This dual optimization mechanism ensures prolonged catalyst life and superior olefin selectivity, particularly ethylene.

The synergy between mechanistic understanding and experimental validation establishes CeO_2-doped SAPO-34 as a superior catalyst for the MTO process. By addressing critical challenges such as coke formation and deactivation, this study provides a comprehensive framework for leveraging CeO_2's redox activity and structural benefits, marking SP-Ce as a pivotal advancement for industrial catalytic applications.

Conflicts of interest

There are no conflicts to declare.

Data availability

The authors state that the data supporting the findings of this study are included in the paper. If raw data files in a different format are required, they can be obtained from the corresponding author upon reasonable request. Source data is supplied with this paper.

Acknowledgements

This work is based upon research funded by Iran National Science Foundation (INSF) under project no. 4027639.

References

1 J. Luo, T. Xiao, C. Liu and Y. Pan, Recent Progress on the Involvement of Formaldehyde in the Methanol-To-Hydrocarbons Reaction, *ChemSusChem*, 2024, e202400884.
2 N. Zhang, S.-L. Chen, R. Zhu and W. Sun, Evolution pathway and role of intermediates acetaldehyde and acetone formed during the methanol-to-olefins reaction, *Energy Fuels*, 2022, **36**(20), 12708–12718.
3 D. Chen, K. Moljord and A. Holmen, A methanol to olefins review: Diffusion, coke formation and deactivation on SAPO type catalysts, *Microporous Mesoporous Mater.*, 2012, **164**, 239–250.
4 M. E. Potter, Down the microporous rabbit hole of silicoaluminophosphates: Recent developments on synthesis, characterization, and catalytic applications, *ACS Catal.*, 2020, **10**(17), 9758–9789.
5 Y. Liu, *et al.*, Critical role of formaldehyde during methanol conversion to hydrocarbons, *Nat. Commun.*, 2019, **10**(1), 1462.
6 K. Hemelsoet, J. Van der Mynsbrugge, K. De Wispelaere, M. Waroquier and V. Van Speybroeck, Unraveling the reaction mechanisms governing methanol-to-olefins catalysis by theory and experiment, *ChemPhysChem*, 2013, **14**(8), 1526–1545.
7 S. Wang, Z. Qin, M. Dong, J. Wang and W. Fan, Recent progress on MTO reaction mechanisms and regulation of acid site distribution in the zeolite framework, *Chem Catal.*, 2022, **2**(7), 1657–1685.
8 D. Zapater, *et al.*, Effect of Thermal, Acid, and Alkaline Treatments over SAPO-34 and Its Agglomerated Catalysts: Property Modification and Methanol-to-Olefin Reaction Performance, *Ind. Eng. Chem. Res.*, 2024, **63**(8), 3586–3599.
9 M. S. Arabahmadi, R. Golhosseini, M. S. Yazd and F. Meshkani, Catalytic performance and hydrogen spillover in Cu/ZnO/Al2O3: Insights from DFT calculations on alkali and alkaline earth oxides promoters for CO2 hydrogenation, *J. CO_2 Util.*, 2025, **99**, 103162.
10 F. Biabangard, J. T. Darian and M. S. Yazd, Oxygenate-mediated catalysis for CO2 hydrogenation: A sustainable path to light olefins, *J. CO_2 Util.*, 2025, **98**, 103149.
11 R. Liu, X. Shao, C. Wang, W. Dai and N. Guan, Reaction mechanism of methanol-to-hydrocarbons conversion: Fundamental and application, *Chin. J. Catal.*, 2023, **47**, 67–92.
12 M. DeLuca, C. Janes and D. Hibbitts, Contrasting arene, alkene, diene, and formaldehyde hydrogenation in H-ZSM-5, H-SSZ-13, and H-SAPO-34 frameworks during MTO, *ACS Catal.*, 2020, **10**(8), 4593–4607.
13 M. Sedighi, M. Ghasemi, M. Sadeqzadeh and M. Hadi, Thorough study of the effect of metal-incorporated SAPO-34 molecular sieves on catalytic performances in MTO process, *Powder Technol.*, 2016, **291**, 131–139.
14 M. Hartmann and L. Kevan, Transition-metal ions in aluminophosphate and silicoaluminophosphate molecular sieves: location, interaction with adsorbates and catalytic properties, *Chem. Rev.*, 1999, **99**(3), 635–664.
15 A. Z. Varzaneh, J. Towfighi and S. Sahebdelfar, Carbon nanotube templated synthesis of metal containing hierarchical SAPO-34 catalysts: impact of the preparation method and metal avidities in the MTO reaction, *Microporous Mesoporous Mater.*, 2016, **236**, 1–12.
16 M. Hartmann and S. Elangovan, Catalysis with microporous aluminophosphates and silicoaluminophosphates containing transition metals, *Advances in Nanoporous Materials*, 2010, vol. 1, pp. 237–312.

17 X. Gong, M. Caglayan, Y. Ye, K. Liu, J. Gascon and A. Dutta Chowdhury, First-generation organic reaction intermediates in zeolite chemistry and catalysis, *Chem. Rev.*, 2022, **122**(18), 14275–14345.
18 B. Liu, *et al.*, Methanol-to-hydrocarbons conversion over MoO 3/H-ZSM-5 catalysts prepared via lower temperature calcination: a route to tailor the distribution and evolution of promoter Mo species, and their corresponding catalytic properties, *Chem. Sci.*, 2015, **6**(9), 5152–5163.
19 H. Huang, M. Yu, Q. Zhang and C. Li, Mechanistic study on the effect of ZnO on methanol conversion over SAPO-34 zeolite, *Catal. Commun.*, 2020, **137**, 105932.
20 J. Zhong, *et al.*, The template-assisted zinc ion incorporation in SAPO-34 and the enhanced ethylene selectivity in MTO reaction, *J. Energy Chem.*, 2019, **32**, 174–181.
21 H. Huang, H. Wang, H. Zhu, S. Zhang, Q. Zhang and C. Li, Enhanced ethene to propene ratio over Zn-modified SAPO-34 zeolites in methanol-to-olefin reaction, *Catal. Sci. Technol.*, 2019, **9**(9), 2203–2210.
22 T. Cordero-Lanzac, *et al.*, Transitioning from Methanol to Olefins (MTO) toward a Tandem CO2 Hydrogenation Process: On the Role and Fate of Heteroatoms (Mg, Si) in MAPO-18 Zeotypes, *JACS Au*, 2024, **4**(2), 744–759.
23 Z. Xu, *et al.*, Enhanced reaction lifetime of a bifunctional catalyst for methanol to olefins by combining formaldehyde decomposition on CeO2, *Catal. Commun.*, 2020, **141**, 106014.
24 J. Zhong, *et al.*, Recent advances of the nano-hierarchical SAPO-34 in the methanol-to-olefin (MTO) reaction and other applications, *Catal. Sci. Technol.*, 2017, **7**(21), 4905–4923.
25 J. Zhong, J. Han, Y. Wei and Z. Liu, Catalysts and shape selective catalysis in the methanol-to-olefin (MTO) reaction, *J. Catal.*, 2021, **396**, 23–31.
26 Z.-P. Hu, J. Han, Y. Wei and Z. Liu, Dynamic evolution of zeolite framework and metal-zeolite interface, *ACS Catal.*, 2022, **12**(9), 5060–5076.
27 M. S. Yazd, S. Motahari, M. R. Rahimpour, S. F. Moorjani and F. S. Bazghaleh, The support effect on the performance of a MOF-derived Co-based nano-catalyst in Fischer Tropsch synthesis, *Nanoscale*, 2024, **16**, 19422–19444.
28 M. Safari, A. Haghtalab and F. A. Roghabadi, Promoting jet fuel production by utilizing a Ru-doped Co-based catalyst of Ru-Co@ C (Zd)@ Void@ CeO 2 in Fischer Tropsch synthesis, *RSC Adv.*, 2023, **13**(50), 35525–35536.
29 E. Aghaei and M. Haghighi, Hydrothermal synthesis of nanostructured Ce-SAPO-34: High-performance and long-lifetime catalyst with various ceria contents for methanol to light olefins conversion, *Microporous Mesoporous Mater.*, 2018, **270**, 227–240.
30 S. Askari, A. B. Siahmard, R. Halladj and S. M. Alipour, Different techniques and their effective parameters in nano SAPO-34 synthesis: A review, *Powder Technol.*, 2016, **301**, 268–287.
31 M. Safari, A. Haghtalab and F. A. Roghabadi, Comprehensive kinetic modeling of the Fischer Tropsch synthesis over the Ru–Co@ C (Zd)@ void@ CeO2 catalyst based on a molecular dynamics evaluated mechanism, *Int. J. Hydrogen Energy*, 2024, **53**, 60–74.
32 M. S. Yazd and J. T. Darian, A bifunctional catalyst for direct CO2 conversion to clean fuels: Mechanistic insights and a comprehensive kinetic model, *Fuel Process. Technol.*, 2024, **266**, 108152.
33 M. Safari, A. Haghtalab and F. A. Roghabadi, Tuning the strong metal support interaction of the Fischer-Tropsch synthesis silica-coated cobalt-based nano-catalyst, *Int. J. Hydrogen Energy*, 2024, **65**, 348–361.
34 M. J. Emami, J. T. Darian and M. S. Yazd, A Green Templated and Nitrogen-Incorporated SAPO-34 Catalyst for Enhanced MTO Performance, *Curr. Res. Green Sustainable Chem.*, 2025, 100463.
35 M. S. Yazd and J. T. Darian, Green and more sustainable catalyst for CO and CO2 hydrogenation, *Energy Convers. Manage.: X*, 2025, 100929.
36 M. Safari Yazd and A. Haghtalab, Kinetic modeling of the Fischer-Tropsch synthesis over the Co@ C (Zd)@ void@ CeO2 catalyst, *Chem. Eng. Commun.*, 2025, 1–16.
37 S. Ren, *et al.*, Enhanced MTO performance over acid treated hierarchical SAPO-34, *Chin. J. Catal.*, 2017, **38**(1), 123–130.
38 K. Mirza, M. Ghadiri, M. Haghighi and A. Afghan, Hydrothermal synthesize of modified Fe, Ag and K-SAPO-34 nanostructured catalysts used in methanol conversion to light olefins, *Microporous Mesoporous Mater.*, 2018, **260**, 155–165.
39 B. Hu, W. Chen, X. Wang, G. Mao and M. Luo, Etching behavior of TEAOH in the post-synthesis of hierarchical SAPO-34, *Res. Chem. Intermed.*, 2023, **49**(2), 619–634.
40 C. Sun, *et al.*, Fabrication of hierarchical ZnSAPO-34 by alkali treatment with improved catalytic performance in the methanol-to-olefin reaction, *C. R. Chim.*, 2018, **21**(1), 61–70.
41 S. R. Venna and M. A. Carreon, Microwave assisted phase transformation of silicoaluminophosphate zeolite crystals, *J. Mater. Chem.*, 2009, **19**(20), 3138–3140.
42 M. Salmasi, S. Fatemi and S. Hashemi, MTO reaction over SAPO-34 catalysts synthesized by combination of TEAOH and morpholine templates and different silica sources, *Sci. Iran.*, 2012, **19**(6), 1632–1637.
43 S. Akhgar, J. Towfighi and M. Hamidzadeh, A green and cost-effective surfactant-assisted synthesis of SAPO-34 using dual microporous templates with improved performance in MTO reaction, *J. Sol-Gel Sci. Technol.*, 2020, **95**, 253–264.
44 T. Zheng, *et al.*, Post synthesis of hierarchical SAPO-34 via citric acid etching: Mechanism of selective desilication, *Microporous Mesoporous Mater.*, 2022, **335**, 111798.
45 E. Aghaei and M. Haghighi, Enhancement of catalytic lifetime of nanostructured SAPO-34 in conversion of biomethanol to light olefins, *Microporous Mesoporous Mater.*, 2014, **196**, 179–190.
46 Y.-L. Zhu, H. Dai, Y. Duan, Q. Chen and M. Zhang, Excellent methanol to olefin performance of SAPO-34 crystal deriving from the mixed micropore, mesopore, and macropore architecture, *Cryst. Growth Des.*, 2020, **20**(4), 2623–2631.

47 T. Doan, K. Nguyen, P. Dam, T. H. Vuong, M. T. Le and H. P. Thanh, Synthesis of SAPO-34 Using Different Combinations of Organic Structure-Directing Agents, *J. Chem.*, 2019, **2019**(1), 6197527.

48 F. Xue, C. Miao, Y. Yue, W. Hua and Z. Gao, Sc2O3-promoted composite of In2O3 and Beta zeolite for direct conversion of bio-ethanol to propylene, *Fuel Process. Technol.*, 2019, **186**, 110–115.

49 A. Parra-Marfil, A. F. Pérez-Cadenas, F. Carrasco-Marín, R. Ocampo-Pérez and E. Bailón-García, Revolutionizing Monolithic Catalysts: The Breakthroughs of Design Control through Computer-Aided-Manufacturing, *Adv. Mater. Technol.*, 2024, 2400064.

50 Z. Dong, W. Chen, K. Xu, Y. Liu, J. Wu and F. Zhang, Understanding the structure–activity relationships in catalytic conversion of polyolefin plastics by zeolite-based catalysts: a critical review, *ACS Catal.*, 2022, **12**(24), 14882–14901.

51 M. S. Yazd, J. T. Darian, F. S. Bazghaleh, M. Pourmand and F. S. Bazghaleh, Identifying and enhancing the spillover of crucial intermediates on the Fischer–Tropsch catalyst: A mechanistic approach, *Fuel Process. Technol.*, 2025, **273**, 108225.

52 M. S. Yazd, A. Haghtalab and F. A. Roghabadi, Screening the footprints of water in the Fischer Tropsch synthesis over a Ru promoted Co-based catalyst supported by ceria,"a mechanistic insight", *Fuel*, 2025, **393**, 134996.

53 A. Abbasi, J. T. Darian, F. S. Bazghaleh and M. S. Yazd, Boosting SAPO-34 catalyst longevity and activity in MTO processes via indium oxide doping: an experimental and theoretical study, *React. Chem. Eng.*, 2025, 12.

54 W. Yu, *et al.*, Synthesis and applications of SAPO-34 molecular sieves, *Chem.–Eur. J.*, 2022, **28**(11), e202102787.

55 T. Kuznetsova and A. Rat'ko, Peculiarities of tetrachloromethane vapor sorption by mesoporous γ-Al 2 O 3 templated at different stages of sol-gel process, *Colloid J.*, 2004, **66**, 709–713.

56 Z. Liu, M. Xu, X. Huai, C. Huang and L. Lou, Ionothermal synthesis and characterization of AlPO4 and AlGaPO4 molecular sieves with LTA topology, *Microporous Mesoporous Mater.*, 2020, **305**, 110315.

57 J. Dai and H. Zhang, Recent advances in catalytic confinement effect within micro/meso-porous crystalline materials, *Small*, 2021, **17**(22), 2005334.

58 G. Zhang and W. Xie, Hierarchical porous SAPO-34 decorated with Mo and W oxides for concurrent transesterification-esterifications for efficient biodiesel production from acidic soybean oil, *Renewable Energy*, 2024, **222**, 119927.

59 P. Wang, D. Yang, J. Hu and G. Lu, Synthesis of SAPO-34 with small and tunable crystallite size by two-step hydrothermal crystallization and its catalytic performance for MTO reaction, *Catal. Today*, 2013, **212**, 62.

60 Q. Chen, *et al.*, Ce regulated surface properties of Mn/SAPO-34 for improved NH 3-SCR at low temperature, *RSC Adv.*, 2020, **10**(66), 40047–40054.

61 J.-W. Mao, X. Bin, Y.-K. Hu, C.-Y. Zhang and H.-M. Meng, Effect of Ce metal modification on the hydrothermal stability of Cu-SAPO-34 catalyst, *J. Fuel Chem. Technol.*, 2020, **48**(10), 1208–1216.

62 N. Zhang, *et al.*, Insight into the Coke Precursor in the Process of the Methanol-to-Olefins Reaction, *Energy Fuels*, 2019, **34**(1), 742–748.

63 A. Hwang and A. Bhan, Deactivation of zeolites and zeotypes in methanol-to-hydrocarbons catalysis: Mechanisms and circumvention, *Acc. Chem. Res.*, 2019, **52**(9), 2647–2656.

64 H. M. Khalafbadam, J. T. Darian and M. S. Yazd, Surface potential charge modulation and sequential etching strategies for optimizing SAPO-34 catalysts in the MTO process: mechanistic insights into catalytic performance, *Appl. Catal., A*, 2025, **700**, 120290.

65 E. N. Al-Shafei, D. R. Brown, S. P. Katikaneni, H. Al-Badairy and O. Muraza, CO2-assisted propane dehydrogenation over of zirconia-titania catalysts: effect of the carbon dioxide to propane ratios on olefin yields, *J. Environ. Chem. Eng.*, 2021, **9**(1), 104989.

66 G. Zhao, Y. Liu, and Y. Lu, From Nano-to Macro-engineering of Nanocomposites and Applications in Heterogeneous Catalysis, in *Advances in Nanostructured Composites*, CRC Press, 2019, pp. 83–109.

67 D. Rojo-Gama, *et al.*, Structure–deactivation relationships in zeolites during the methanol–to-hydrocarbons reaction: Complementary assessments of the coke content, *J. Catal.*, 2017, **351**, 33–48.

68 Q. Wang, *et al.*, Effect of kaolin calcined temperature on the preparation and crystallization mechanism of SAPO-34 molecular sieve for methanol-to-olefins performance, *Microporous Mesoporous Mater.*, 2024, **369**, 113037.